

Electron characteristics and dynamics in sub-millimeter pulsed atmospheric dielectric barrier discharge

Junlin Fang(方骏林), Yarong Zhang(张亚容), Chenzi Lu(卢陈梓), Lili Gu(顾莉莉), Shaofeng Xu(徐少锋), Ying Guo(郭颖), and Jianjun Shi(石建军)
Citation: Chin. Phys. B, 2024, 33 (**1**): 015201. DOI: 10.1088/1674-1056/ad0118
Journal homepage: http://cpb.iphy.ac.cn; http://iopscience.iop.org/cpb

What follows is a list of articles you may be interested in

Features of transport induced by ion-driven trapped-electron modes in tokamak plasmas

Hui Li(李慧), Ji-Quan Li(李继全), Feng Wang(王丰), Qi-Bin Luan(栾其斌),Hong-En Sun(孙宏恩), and Zheng-Xiong Wang(王正汹)
Chin. Phys. B, 2023, 32 (**7**): 075206. DOI: 10.1088/1674-1056/acae7e

Correction of intense laser-plasma interactions by QED vacuum polarization in collision of laser beams

Wen-Bo Chen(陈文博) and Zhi-Gang Bu(步志刚)
Chin. Phys. B, 2023, 32 (**2**): 025204. DOI: 10.1088/1674-1056/ac70b3

Ignition dynamics of radio frequency discharge in atmospheric pressure cascade glow discharge

Ya-Rong Zhang(张亚容), Qian-Han Han(韩乾翰), Jun-Lin Fang(方骏林), Ying Guo(郭颖), and Jian-Jun Shi(石建军)
Chin. Phys. B, 2023, 32 (**2**): 025201. DOI: 10.1088/1674-1056/ac673d

Role of the zonal flow in multi-scale multi-mode turbulence with small-scale shear flow in tokamak plasmas

Hui Li(李慧), Jiquan Li(李继全), Zhengxiong Wang(王正汹), Lai Wei(魏来), and Zhaoqing Hu(胡朝清)
Chin. Phys. B, 2022, 31 (**6**): 065207. DOI: 10.1088/1674-1056/ac6011

Numerical study of the effect of water content on OH production in a pulsed-dc atmospheric pressure helium-air plasma jet

Mu-Yang Qian(钱沐杨), Cong-Ying Yang(杨从影), Zhen-dong Wang(王震东), Xiao-Chang Chen(陈小昌), San-Qiu Liu(刘三秋), De-Zhen Wang(王德真)
Chin. Phys. B, 2016, 25 (**1**): 015202. DOI: 10.1088/1674-1056/25/1/015202

Electron characteristics and dynamics in sub-millimeter pulsed atmospheric dielectric barrier discharge

Junlin Fang(方骏林)[1], Yarong Zhang(张亚容)[1], Chenzi Lu(卢陈梓)[1], Lili Gu(顾莉莉)[1], Shaofeng Xu(徐少锋)[1], Ying Guo(郭颖)[1,†], and Jianjun Shi(石建军)[2,‡]

[1] *College of Science, Donghua University, Shanghai* 201620, *China*
[2] *Yiwu Research Institute of Fudan University, Yiwu* 322099, *China*

(Received 2 August 2023; revised manuscript received 18 September 2023; accepted manuscript online 7 October 2023)

The discharge characteristics and mechanism of sub-millimeter pulsed dielectric barrier discharge in atmospheric-pressure helium are investigated experimentally and theoretically, demonstrating that when the discharge gap distance is reduced from 1.00 mm to 0.20 mm, the discharge ignition time is reduced to approximately 40 ns and discharge intensity is enhanced in terms of the discharge optical emission intensity and density of the plasma species, (energetic electrons with energy above 8.40 eV). The simulated results show that as the discharge gap distance is further reduced to 0.10 mm, the number of energetic electrons decreases, which is attributable to the contraction of plasma bulk regime and reduction of electron density in the discharge bulk. Conversely, the proportion of energetic electrons to the total electrons in the discharge monotonically increases as the discharge gap distance is reduced from 1.00 mm to 0.10 mm. It is proposed that a gap distance of 0.12 mm is optimal to achieve a high concentration and proportion of energetic electrons in sub-millimeter pulsed atmosphere dielectric barrier discharge.

Keywords: sub-millimeter pulsed discharge, plasma simulation, electron dynamics and sheath

PACS: 52.20.–j, 52.25.–b, 52.40.Kh **DOI:** 10.1088/1674-1056/ad0118

1. Introduction

Atmospheric-pressure plasmas have attracted significant attention owing to their potential applications in biomedical sterilisation, environmental treatment, and material processing.[1–10] Among the discharge excitations with repetition frequencies from DC to microwaves, sub-microsecond pulsed voltage in the kilohertz range is preferred for its high discharge power consumption efficiency[11] and generation of reactive plasma species.[12] In atmospheric-pressure pulsed discharge, two discharge events are ignited in the rising and falling phases of the pulse voltage,[13] which are generated by overvoltage and develop in the form of fast ionising waves.[14] This ensures high discharge stability and reactivity in terms of electron density and electron energy in atmospheric pulsed discharges.[15] The energetic electrons produced during discharge are responsible for the excitation and dissociation of the working gases from the material processing of deposition and etching,[16] which suggests that the electron energy distribution function must be considered, even in atmospheric-pressure reactive plasma.[17,18] Given that a reduced discharge gap distance can enhance the electric field and shrink the plasma bulk regime, a high concentration and proportion of energetic electrons can be achieved in sub-millimeter discharges.[17–19]

In the present study, the discharge characteristics of a sub-millimeter pulsed atmospheric dielectric barrier discharge were investigated experimentally by using electrical and optical diagnostics. The discharge mechanism in terms of electron dynamics was investigated by numerical simulations, in which the discharge ignition and sheath characteristics in terms of the sheath voltage and thickness were presented to discuss the production of energetic electrons in the discharge.

2. Experimental setup and numerical model

The experimental setup and the schematic diagram of the simulation domain of the two-dimensional (2D) self-consistent numerical model are shown in Fig. 1. The reactor consists of two copper rod electrodes with diameter of 1.00 mm covered with quartz tubes, whose inner and outer diameters are 1.00 mm and 2.00 mm, respectively, and the gas gap distance is varied from 1.00 mm to 0.20 mm. One of the electrodes is powered by a pulse power supply capable of generating sub-microsecond high-voltage pulses with amplitude and repetition frequencies of up to 20 kV and 10 kHz, respectively.

Waveforms of the applied voltage and discharge current were captured using a voltage probe (Tektronix P6015A) and a current probe (Pearson 2877) and collected using a 4-channel

†Corresponding author. E-mail: guoying@dhu.edu.cn
‡Corresponding author. E-mail: jianjunshi@gmail.com

© 2024 Chinese Physical Society and IOP Publishing Ltd

broadband digital oscilloscope (Tektronix DP04104). The discharge images and optical emission spectra were obtained using an ICCD camera (Andor iStar DH720) and spectrometer (Andor SR750).

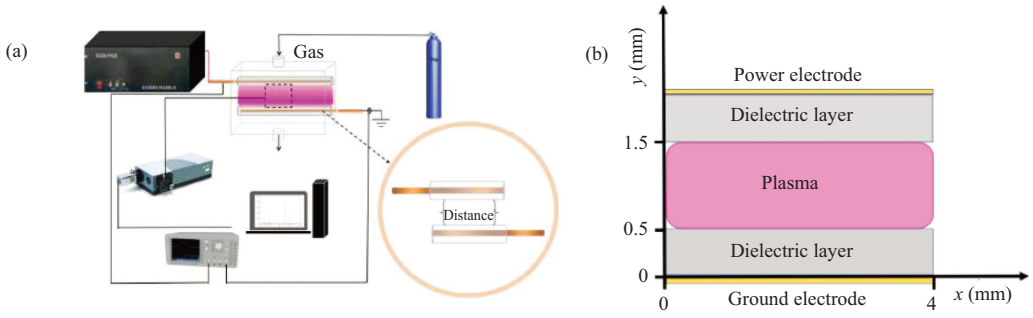


Fig. 1. Experimental setup and two-dimensional schematic diagram of simulation domain.

Table 1. Elementary reaction and rate coefficients.

Reaction	Rate coefficients ($cm^3 \cdot s^{-1}$)
$He + e \rightarrow He^* + e$	$2.308 \times 10^{-10} T_e^{0.31} \exp\left(-\frac{2.297 \times 10^5}{T_e}\right)$
$He + e \rightarrow He^+ + 2e$	$2.584 \times 10^{-12} T_e^{0.68} \exp\left(-\frac{2.854092 \times 10^5}{T_e}\right)$
$He^* + e \rightarrow He^+ + 2e$	$4.661 \times 10^{-10} T_e^{0.6} \exp\left(-\frac{5.546 \times 10^4}{T_e}\right)$
$He_2^+ + e \rightarrow He^* + He$	$5.386 \times 10^{-7} T_e^{-0.5}$
$He^+ + 2He \rightarrow He_2^+ + He$	1.1×10^{-31}
$He^* + 2He \rightarrow He_2^* + He$	1.3×10^{-33}
$He^* + e \rightarrow He + e$	$1.099 \times 10^{-11} T_e^{0.31}$
$He_2^* + e \rightarrow He_2^+ + 2e$	$1.268 \times 10^{-12} T_e^{0.71} \exp\left(-\frac{3.945 \times 10^4}{T_e}\right)$
$He^* + He^* \rightarrow He^+ + He + e$	2.7×10^{-10}

The thickness and relative permittivity of the dielectric layer were fixed at 0.50 mm and 10, respectively, and the length along the axis was fixed at 4.00 mm. Table 1 presents the elementary reactions and their reaction rates considered in the mode,[20–22] where T_e is the mean electron energy. Electrons (e), helium ions (He^+), ionized helium molecules (He_2^+), excited helium atoms (He^*), and excited helium molecules (He_2^*) can be determined by the particle continuity, as shown in equation.

The number density of plasma species are obtained by solving the continuity equations[20–22]

$$\frac{\partial n}{\partial t} + \frac{\partial \Gamma_x}{\partial x} + \frac{\partial \Gamma_y}{\partial y} = S, \tag{1}$$

where n, Γ, and S are the number density, flux, and sources of the plasma species, respectively, x and y correspond to the axial and radial directions, respectively. The fluxes of ions and electrons are

$$\Gamma_{i,e}(x) = \pm \mu_{i,e} n_{i,e} E_x - D_{i,e} \frac{\partial n_{i,e}}{\partial x}, \tag{2}$$

$$\Gamma_{i,e}(y) = \pm \mu_{i,e} n_{i,e} E_y - D_{i,e} \frac{\partial n_{i,e}}{\partial y}, \tag{3}$$

where i and e denote ion and electron, respectively, and μ and D denote the coefficients of mobility and diffusivity, respectively. The electrical field E can be obtained by solving Poisson's equation

$$\varepsilon_0 \left(\frac{\partial E_x}{\partial x} + \frac{\partial E_y}{\partial y} \right) = e \left(\sum_p n_{i,p} - n_e \right), \tag{4}$$

where ε_0 and e denote the vacuum permittivity and elementary charge, respectively. Electron mean energy ε can be calculated as follows:

$$\frac{\partial n_e \varepsilon}{\partial x} = -\frac{\Gamma_\varepsilon}{\partial x} + e\Gamma_e E - K_{L,ij}(\varepsilon) n_i n_j - 3\frac{m_e}{m_{neut}} N K_{mt} n_e k (T_e - T_{neut}), \tag{5}$$

where T is the temperature of a plasma species, and m is the mass of a plasma species. $K_{i,j}$ and $K_{L,ij}$ are the reaction rate and the energy gain/loss rate attributed to the reaction between species i and j, respectively. K_{mt} is the momentum-transfer

frequency corresponding to the elastic collision between electrons and background gas atoms.

The boundary condition for electrons and ions is expressed as

$$\Gamma_e = -\gamma\Gamma_i, \tag{6}$$

where the secondary electron emission coefficient γ was set to 0.02, and the energy of the secondary electrons from the electrodes was fixed at 1.00 eV.

3. Results and discussion

3.1. Discharge ignition

Typical waveforms of the current density of the pulsed discharge measured in experiments and simulation with a gap distance of 1.00 mm are shown in Fig. 2.

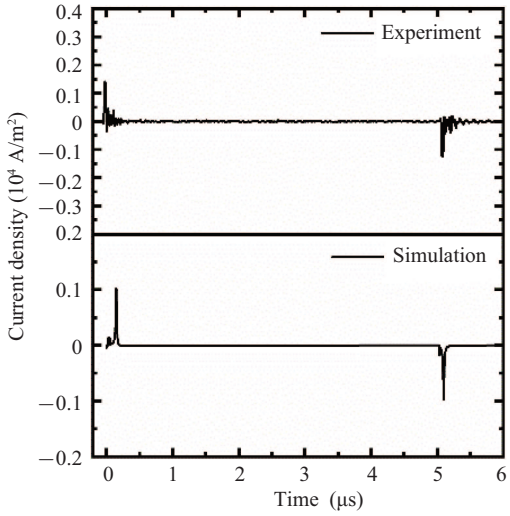


Fig. 2. Waveforms of current density measured in experiments and simulation.

The pulse voltage has a pulse duration of 5.0 μs, with a rising and falling duration of 50 ns and a repetitive frequency and amplitude of 3.0 kHz and 1.60 kV in the experiments, respectively.

As presented in Fig. 2, two pulse discharge events occur, which correspond to the rising and falling phase discharges with discharge current densities of 0.14×10^4 A/m^2 and 0.13×10^4 A/m^2 in the experiment, respectively, and 0.10×10^4 A/m^2 and 0.097×10^4 A/m^2 in the simulation, respectively.

Figures 3(a) and 3(b) show the normalized spatiotemporal distribution discharge from 0 μs–6.0 μs in the experiment and simulation, respectively. The exposure time in Fig. 3(a) and the time interval between two consecutive images were set to 10 ns. At the time instant of 0.17 μs in the experiment, as shown in Fig. 3(a), the pulse discharge gradually moved from the pulse electrode (0 mm) to the ground electrode (1 mm), and it reached the ground electrode at 0.32 μs. At the time instant of 5.30 μs, the pulse was discharged on the falling edge, and it reached the pulse electrode at 5.46 μs. At the time instant of 0.2 μs in the simulation of Fig. 3(b), the pulse discharge gradually moved from the pulse electrode to the ground electrode; it reached the ground electrode at 0.3 μs. At the time instant of 5.1 μs, the pulse was discharged on the falling edge; it reached the pulse electrode at 5.2 μs. In experiments and simulations, both the rising and falling edge discharges of the pulse discharge were completed within 0 μs–6 μs.

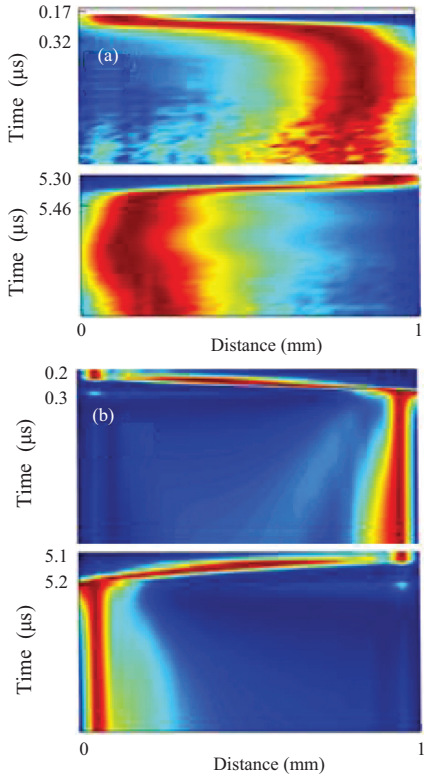


Fig. 3. The spatiotemporal evolution of pulse discharge: (a) experiments and (b) numerically simulated results.

Figure 4(a) presents the relationship between the ignition time and discharge gap distance. The discharge image was captured by an ICCD camera with an exposure time and time interval between two consecutive images of 10 ns. The discharge ignition time was determined from the glow of the discharge image in the experiments and the increase in the discharge current density in the simulation.[23] As the discharge gap decreases from 1.00 mm to 0.20 mm, the ignition time is shortened from 190 ns to 150 ns in the experimental measurements and from 126 ns to 90 ns in the numerical simulation, which are consistent with the findings of other studies.[24,25] The discharge ignition time was shortened by approximately 40 ns, suggesting that the pulsed discharge could be enhanced with the same applied pulse voltage by reducing the gap distance. The discrepancy of discharge ignition time measured in experiments and determined in simulation can be attributed to the detection limit of ICCD camera on discharge optical

emission intensity and the gas impurity is not considered in numerical model.

Figure 4(b) shows the average electron energy and electric field across the discharge gap at the time of discharge ignition. As the discharge gap decreases from 1.00 mm to 0.20 mm, the average electric field increases from 0.71×10^6 V/m to 2.05×10^6 V/m, and the average electron energy increases from 4.50 eV to 7.07 eV. The average electron energy for the 0.20 mm gap was 1.57 times higher than that for a discharge gap of 1.00 mm, which can be attributed to the enhancement of the electric field.

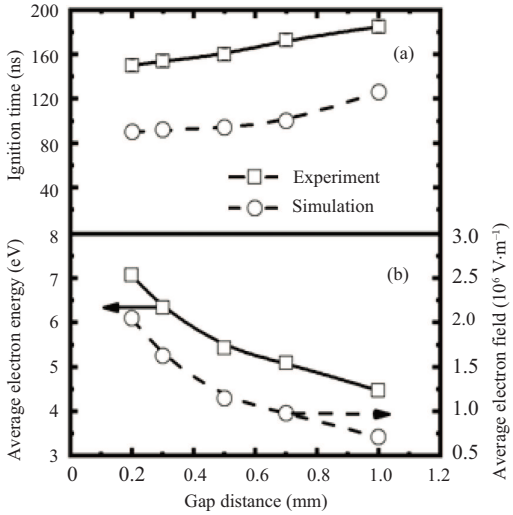


Fig. 4. (a) Dependence of ignition time on discharge gap, (b) the average electron energy and electric field in plasma at the instants of discharge ignition.

3.2. Discharge characteristics and dynamics at the instants of discharge current peaks

The discharge image intensity and optical emission spectrum (OES) at 706 nm measured experimentally at the time of the discharge current peaks are shown in Fig. 5.

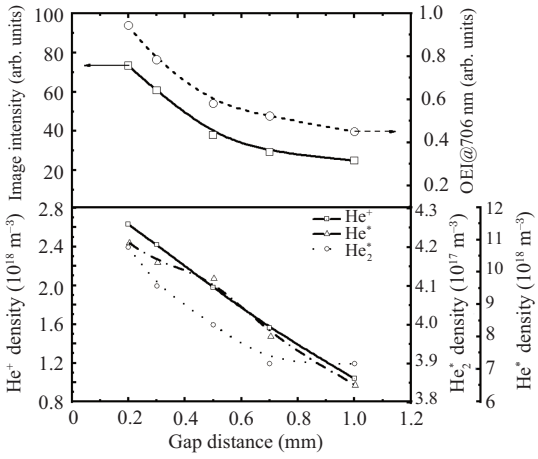


Fig. 5. (a) Measured image intensity and optical emission intensity at 706 nm, (b) simulated density of He^+, He^*, He_2^* at the time of discharge current peaks.

The discharge image and OES at 706 nm were obtained with an exposure time of 1 s. As the discharge gap decreases from 1.00 mm to 0.20 mm, the image intensity increases from 24.89 to 73.36, a factor of 2.95.

The simulated helium ion density is used to compare the experimentally measured light emission intensity from the discharge,[26] which increases from 1.04×10^{18} m^{-3} to 2.63×10^{18} m^{-3} with the reduction of gap distance from 1.00 mm to 0.20 mm and is consistent with the dependence of discharge image intensity on discharge gap distance. He^* density increases from 6.50×10^{18} m^{-3} to 10.90×10^{18} m^{-3} and He_2^* density increases from 3.9×10^{17} m^{-3} to 4.20×10^{17} m^{-3} with the reduction of gap distance from 1.00 mm to 0.20 mm. The intensity of the optical emission line at 706 nm indicates the presence of energetic electrons (above 2.9 eV) in the discharge. With the improved discharge intensity in terms of discharge image intensity and helium ion density, the optical emission intensity at 706 nm increases from 0.45 to 0.94 with the reduction of gap distance from 1.00 mm to 0.20 mm, as shown in Fig. 5(a). This suggests that the density of the generated energetic electrons is enhanced with a reduced discharge gap distance in the sheath region.

Figure 6 shows the temporal evolution of the electric field, electron temperature, e and the formation process of sheath. Figure 6(a) the spatial distribution of the electric field at intervals of 1 mm in the simulation. At 0.1 μs, there is no discharge in the gap, and the electric field exhibits a linear growth trend from 6.1×10^5 V/m to 7.7×10^5 V/m. At 0.267 μs, the ionization wave propagates to the middle region of the gap. At this moment, in the area passed by the ionization wave, the electric field rapidly decreases. Simultaneously, the electric field between the head of the ionization wave and the ground electrode (0.50 mm) rapidly increases to 17.9×10^5 V/m. At 0.294 μs, the discharge approaches its maximum strength.

The maximum electric field in the gap increases to 29.1×10^5 V/m in the sheath region. Subsequently, as the reaction progresses, the maximum electric field in the sheath region gradually decreases from 29.1×10^5 V/m to 12.8×10^5 V/m. Figure 6(b) represents the spatiotemporal evolution of electron temperature. At 0.1 μs, the spatial electron energy is uniformly distributed, with values ranging between 4 eV to 5 eV in the gap. At 0.267 μs, the ionization wave propagates to the middle region of the gap. At this moment, in the area passed by the ionization wave, the electric energy rapidly decreases to 1.0 eV–2.0 eV. Simultaneously, the electric energy between the head of the ionization wave and ground electrode rapidly increases to 6.7 eV. At 0.294 μs, the discharge approaches its maximum strength. The maximum electric energy in the gap increases to 8.3 eV in the sheath region. Subsequently, as the reaction progresses, the maximum electric energy in the sheath

region gradually decreases from 8.3 eV at 0.294 μs to 5.2 eV at 0.324 μs.

Figure 6(c) shows the spatiotemporal evolution of electron density. At 0.1 μs, the spatial electron density ranges between 2×10^{14} m^{-3}–20×10^{14} m^{-3} in the gap. At 0.267 μs, the ionization wave propagates to the middle region of the gap. Simultaneously, at the head of the ionization wave, the electron density rapidly increases to 2.1×10^{17} m^{-3}. At 0.294 μs, the discharge approaches its maximum strength. The maximum electric density in the gap increases to 1.08×10^{18} m^{-3} in the sheath boundary. Subsequently, as the reaction progresses, the maximum electric density gradually decreases from 1.19×10^{18} m^{-3} at 0.304 μs to 1.08×10^{18} m^{-3} at 0.324 μs.

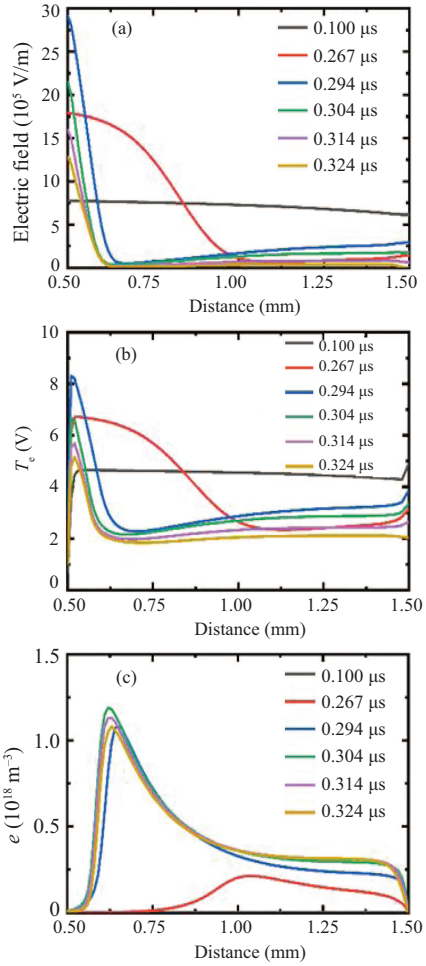


Fig. 6. (a) Temporal evolution of electric field in simulation, (b) temporal evolution of electron temperature, and (c) temporal evolution of electron spatial distribution.

Figure 7 shows the spatial distribution of the gas potential, electron energy, electrons density, and helium ions at 0.294 μs. There is a significant drop in the sheath region, and electrons are mainly concentrated in the area outside the sheath boundary.

During the discharge process, the electron energy distribution trend consistently follows that of the electric field distribution, with electrons primarily being generated at the head of the ionization wave. Energetic electrons are generated in the sheath region. As the ionization wave propagates, the sheath voltage gradually increases, leading to a compression of the sheath structure. This compression also causes changes in the number of energetic electrons within the sheath, ultimately affecting the overall intensity of the discharge.

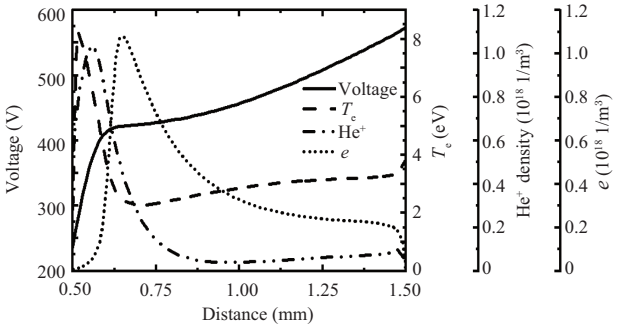


Fig. 7. Spatial distribution of the gas potential, electron energy, electrons density, and helium ions at 0.294 μs.

The sheath region formed above the electrode surface plays an important role in electron dynamics during discharge. Figure 8 shows the discharge-gap distance-dependent sheath characteristics in terms of the sheath thickness and sheath voltage as calculated in the simulation. As shown in Fig. 8, as the discharge gap is reduced from 1.00 mm to 0.30 mm, the sheath thickness decreases gradually from 95.04 μm to 82.65 μm and the sheath voltage increases from 154.00 V to 197.77 V.

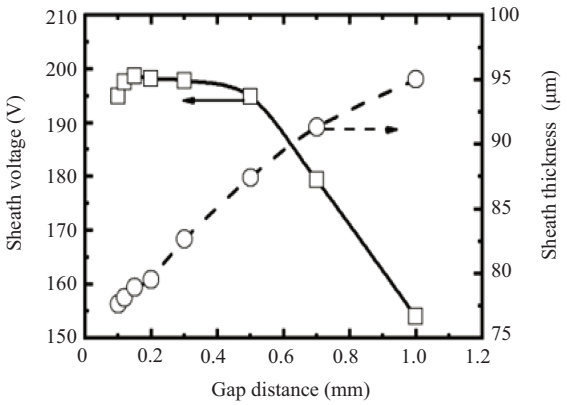


Fig. 8. Sheath thickness and sheath voltage as functions of discharge gap distance at discharge current peaks.

The reductions in both sheath thickness and sheath voltage suggest an enhancement of the electric field in the sheath region. With further reductions of the gap distance from 0.30 mm to 0.12 mm, the sheath thickness continues decreasing from 82.65 μm to 78.14 μm, suggesting that the discharge gap distance approaches the sheath thickness and the sheath voltage maintains a magnitude between 197.00 V and 199.00 V. When the discharge gap is reduced to 0.10 mm, the sheath voltage is reduced to 194.00 V, indicating that the enhancement of the electric field in the sheath region is limited

because the discharge gap distance is close to the sheath thickness.

The discharge reactivity is primarily determined by the concentration and proportion of energetic electrons in the discharge. In Fig. 9, the number of energetic electrons is obtained by integrating the electron density with energies equal to or greater than 8.4 eV in the discharge domain, as shown in Fig. 1(b). The ratio of energetic electrons to total electrons (R) in the discharge is also presented. With the reduction of the discharge gap distance from 1.00 mm to 0.10 mm, R increases from 0.01% to 3.84%, especially when the discharge gap distance is less than 0.20 mm. This can be attributed to the enhancement of the electric field in the sheath region with a reduction in the discharge gap distance, where energetic electrons are generated, as shown in Fig. 5. This is also because of the elevated proportion of the sheath thickness to discharge gap distance as the thickness of the plasma bulk region is reduced by the reduction in the discharge gap distance, where the electron density is high and the electron energy is low.[27]

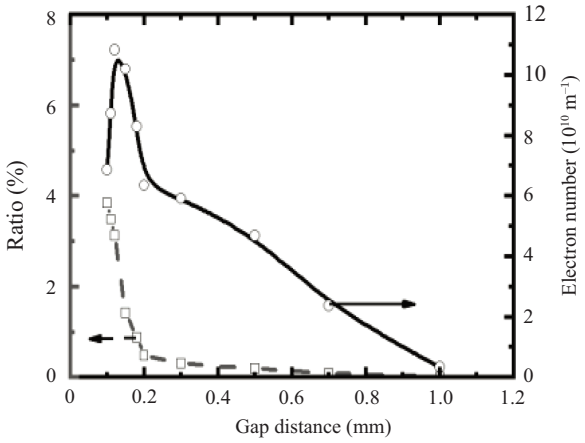


Fig. 9. The number and proportion of energetic electrons as functions of discharge gap distance at discharge current peaks.

Conversely, when the discharge gap is reduced from 1.00 mm to 0.12 mm, the population of energetic electrons increases from 0.34×10^{10} m^{-1} to 1.08×10^{11} m^{-1} owing to the elevated proportion of energetic electrons and discharge intensity, as shown in Fig. 5. It is interesting to note that the population of energetic electrons declines to 6.87×10^{10} m^{-1} at a discharge gap of 0.10 mm. As shown in Fig. 9, when the discharge gap distance is less than 0.12 mm, the sheath voltage decreases, which suggests that the generation of energetic electrons declines, although the proportion of energetic electrons continues to increase.

As shown in Fig. 10, it was observed that the peak moments of OES at 777 nm and 336 nm at 170 ns appeared 10 ns–30 ns later than the one at 706 nm (150 ns) at a distance of 0.2 mm in the experiment.

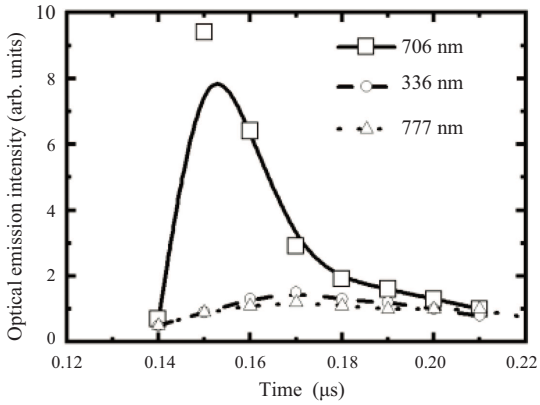


Fig. 10. Spectral evolution of OES at 777 nm, 336 nm, and 706 nm.

Figure 11 shows the spatiotemporal evolution of Te, He^+, He^*, He_2^* at a distance of 0.2 mm in the simulation. At 0.124 μs, the helium ions reach the maximum density (2.6×10^{18} m^{-3}), which then gradually decrease to 0.058×10^{18} m^{-3} (0.18 μs). The electron temperature gradually decreases from its maximum value of 10.5 eV (0.124 μs) to 1.6 eV (0.18 μs). He_2^* increases from 0.36×10^{17} m^{-3} (0.124 μs) to 0.88×10^{17} m^{-3} (0.18 μs). He^* increases from 1.22×10^{19} m^{-3} (0.124 μs) to 1.3×10^{19} m^{-3} (0.13 μs) and then decreases to 1.27×10^{19} m^{-3} (0.18 μs).

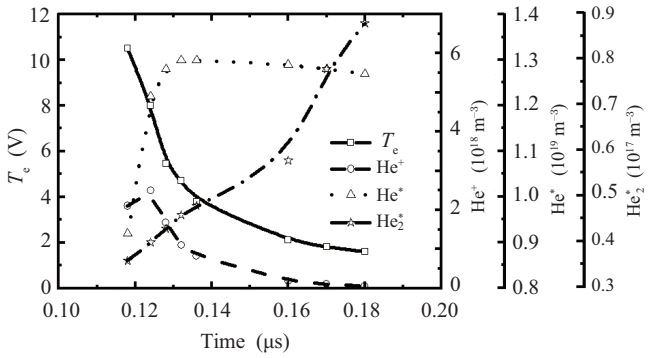


Fig. 11. Spatiotemporal evolution of Te, He^+, He^*, and He_2^*.

After the moment of strongest discharge, from 0.124 μs to 0.18 μs both the electron temperature and density of helium ions rapidly decrease which indicates the spectral delay in Fig. 10 is not caused by energetic electrons.

The density of He^* is larger than that of He_2^* by two orders of magnitude. After 0.13 μs, the density of He^* starts to decreases in a similar trend to OES at 777 nm and 336 nm in Fig. 10. It can be inferred that the variations in the emission spectrum are mainly influenced by the active particles (He^*). The energetic electrons generated in the sheath region are the main raw material for producing active particles.

4. Conclusions

The discharge characteristics and mechanism of submillimeter pulsed dielectric barrier discharge were studied experimentally and theoretically using a two-dimensional self-consistent fluid model. With a reduction in the discharge gap

distance from 1.00 mm to 0.20 mm, the discharge ignition time is reduced and discharge intensity is enhanced in terms of discharge image intensity and optical emission spectrum intensity at 706 nm. The simulation results show that the number of energetic electrons in the discharge gradually increases as the discharge gap distance is reduced from 1.00 mm to 0.12 mm and declines with the discharge gap distance with further reductions to 0.10 mm. This is attributed to the enhancement of the electric field in the sheath region and contraction of plasma bulk regime in the discharge. Meanwhile, the proportion of energetic electrons to total electrons in the discharge increases further as the discharge gap distance is reduced from 1.00 mm to 0.10 mm with the enhancement of the electric field.

Acknowledgement

Project supported by the National Natural Science Foundation of China (Grant Nos. 12175036 and 11875104).

References

[1] Borcia G, Anderson C A and Brown N M D 2003 *Plasma Sources Sci. Technol.* **12** 3354
[2] Barnes B K, Ouro-Koura H, Derickson J, *et al.* 2021 *Am. J. Phys.* **89** 372
[3] Teramoto Y, Fukumoto Y, Ono R and Oda T 2011 *IEEE Trans. Plasma Sci.* **39** 2218
[4] Borcia G, Anderson C A and Brown N M D 2005 *Plasma Sources Sci. Technol.* **14** 259
[5] Park G Y, Park S J, Choi M Y, Koo I G, *et al.* 2012 *Plasma Sources Sci. Technol.* **21** 043001
[6] Bogaerts A, Aerts R, Snoeckx R, *et al.* 2012 *J. Phys.: Conf. Ser.* **399** 012011
[7] Misra N, Bhatt S, Khonsari F A and Kumar V 2021 *Plasma Process. Polym.* **18** e2000215
[8] Xu S, Jirasek V and Lukes P 2023 *Chemistryselect* **8** e202203937
[9] Xu S, Jirasek V and Lukes P 2020 *J. Phys. D: Appl. Phys.* **53** 275204
[10] Zhang Y R, Han Q H, Fang J L, *et al.* 2023 *Chin. Phys. B* **32** 025201
[11] Tao Shao, Cheng Zhang, Ruixue Wang, *et al.* 2016 *High Voltage Engineering* **42** 685
[12] Martens T, Bogaerts A and van Dijk J 2010 *Appl. Phys. Lett.* **96** 131503
[13] Walsh J L and Kong M G 2006 *Appl. Phys. Lett.* **89** 231503
[14] Tarasenko V F, Lomaev M I and Sorokin D A 2010 *IEEE Electron Dev. Lett.*
[15] Williamson J M, Trump D D, Bletzinger P, *et al.* 2006 *J. Phys. D: Appl. Phys.* **39** 4400
[16] Wang D H, Wang S X, Nie Z W, *et al.* 2022 *Plasma Sources Sci. Technol.* **31** 045012
[17] Lodygin A N, Portsel L M, Beregulin E V, *et al.* 2019 *J. Appl. Phys.* **126** 173302
[18] Sugawara H 2017 *Plasma Sources Sci. Technol.* **26** 044002
[19] Wei L, Hu Z, Zhang Y and Yang C 2010 *OZONE-Sci. Eng.* **32** 444
[20] Zhang Y R, Han Q H, Guo Y, *et al.* 2021 *Acta Phys. Sin.* **70** 095202 (in Chinese)
[21] Han Q, Guo Y, Zhang Y, Zhang J, *et al.* 2021 *AIP Adv.* **11** 025021
[22] Zhang Y, Fang J, Xu S, *et al.* 2023 *Plasma Sources Sci. Technol.* **32** 035003
[23] Qian Y J, Ding K, Song S T, *et al.* 2012 *Plasma Phys.* **52** 289
[24] Lu X, Wu S, Chu P K, Liu D, *et al.* 2011 *Plasma Sources Sci. Technol.* **20** 065009
[25] Donko Z, Derzsi A, Vass M, *et al.* 2018 *Plasma Sources Sci. Technol.* **27** 104008
[26] Sakiyama Y, Graves D B and Stoffels E 2008 *J. Phys. D: Appl. Phys.* **41** 095204
[27] Song S, Guo Y, Choe W, Zhang J, *et al.* 2012 *Phys. Plasmas* **19** 123508